3D Hinge Transport in Acoustic Higher-Order Topological Insulators

Qiang Wei,[1,2] Xuewei Zhang,[1,2] Weiyin Deng,[3] Jiuyang Lu,[3] Xueqin Huang,[3] Mou Yan,[3] Gang Chen,[1,2,4,*] Zhengyou Liu,[5,6,†] and Suotang Jia[1,2]

[1]*State Key Laboratory of Quantum Optics and Quantum Optics Devices, Institute of Laser spectroscopy, Shanxi University, Taiyuan 030006, China*

[2]*Collaborative Innovation Center of Extreme Optics, Shanxi University, Taiyuan, Shanxi 030006, China*

[3]*School of Physics and Optoelectronics, South China University of Technology, Guangzhou, Guangdong 510640, China*

[4]*Collaborative Innovation Center of Light Manipulations and Applications, Shandong Normal University, Jinan 250358, China*

[5]*Key Laboratory of Artificial Micro- and Nanostructures of Ministry of Education and School of Physics and Technology, Wuhan University, Wuhan 430072, China*

[6]*Institute for Advanced Studies, Wuhan University, Wuhan 430072, China*

(Received 1 July 2021; revised 22 October 2021; accepted 22 November 2021; published 17 December 2021)

The discovery of topologically protected boundary states in topological insulators opens a new avenue toward exploring novel transport phenomena. The one-way feature of boundary states against disorders and impurities prospects great potential in applications of electronic and classical wave devices. Particularly, for the 3D higher-order topological insulators, it can host hinge states, which allow the energy to transport along the hinge channels. However, the hinge states have only been observed along a single hinge, and a natural question arises: whether the hinge states can exist simultaneously on all the three independent directions of one sample? Here we theoretically predict, numerically simulate, and experimentally observe the hinge states on three different directions of a higher-order topological phononic crystal, and demonstrate their robust one-way transport from hinge to hinge. Therefore, 3D topological hinge transport is successfully achieved. The novel sound transport may serve as the basis for acoustic devices of unconventional functions.

DOI: 10.1103/PhysRevLett.127.255501

Transport is one of the most fundamental and important notions in condensed-matter physics and material science, and it lays the foundations for almost all devices in application [1–4]. The emergence of topological insulators (TIs) provides an unprecedented opportunity for discovering the state-of-the-art transport behaviors of electrons [5–7] or waves [8–15], overcoming the conventionals, thanks to the topological-protected boundary states they host. The boundary states, which can survive the disorders and impurities, exhibit the robust one-way feature [6,7]. This shows great promise in low-loss devices of electronic and classical wave systems, such as thermoelectric converter [16,17], topological negative refraction [18,19], and topological laser [20].

Of special interest recently is the higher-order TIs, which respect a generalized bulk-boundary correspondence. It states that the d D nth-order TIs possess the boundary states of $(d-n)$ D [21–26]. In particular, for the 3D second-order TI, there exist the topological-protected hinge states [27], which localize on the hinges of the system. To date, the hinge states have only been observed along single hinges [28,29]. It raises a natural question: whether the hinge states can exist simultaneously along all the three independent directions in the higher-order TIs? Recently, such hinge states have been proposed theoretically [30–37], but it is a great challenge to experimentally observe these states and associated 3D one-way transport [38].

In this Letter, we theoretically predict, numerically simulate, and experimentally observe the helical hinge states along three independent directions in a higher-order topological phononic crystal (PC). Specifically, it is constructed by stacking a bilayer hexagonal lattice, with opposite on-site energies for the two layers and different intracell and intercell layer couplings. By interchanging the on-site energies of the bilayer or the intracell and intercell layer couplings, four different phases are obtained, which possess gapped surface and interface states. The Jackiw-Rebbi mechanism [39] results in the hinge states along all the three independent directions, as desired. More importantly, based on these independent hinge states, we demonstrate the 3D robust one-way transport from hinge to hinge. The theoretical, simulated, and experimental results are in good agreement. Our work not only unveils the exotic topological states of matter, but also opens an avenue in the design of new devices.

We first introduce a tight-binding model with a unit cell hosting four sites A_i (magenta spheres) and B_i (purple spheres), where A, B denote the sublattices of each layer and $i = 1, 2$ is the layer degree of freedom [left panel in Fig. 1(a)]. The sites A_1 and B_2 have the same on-site energy

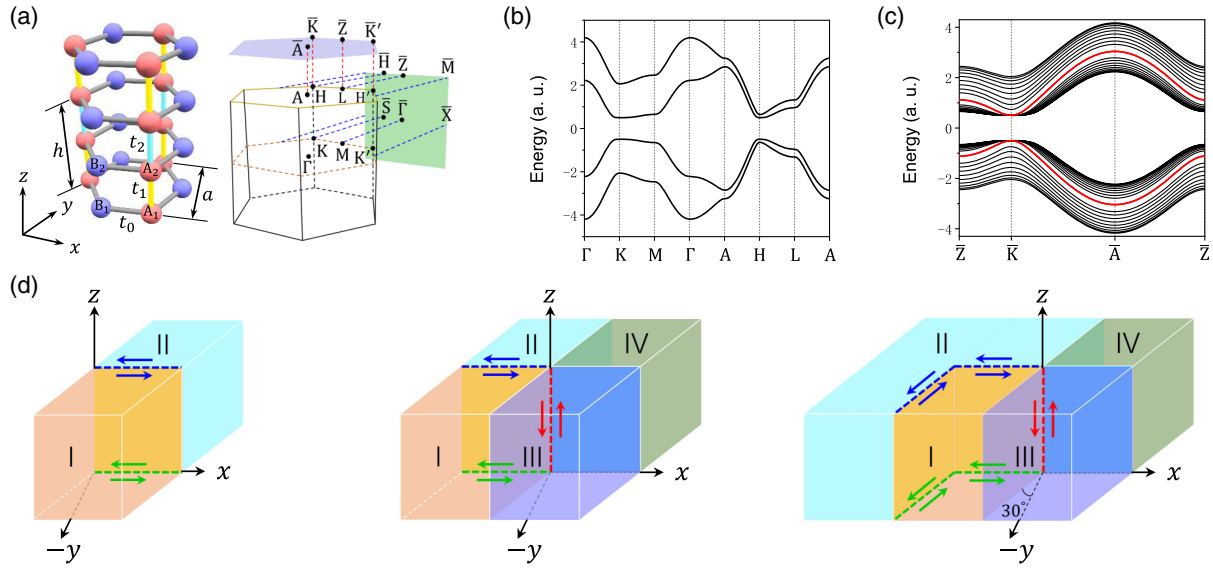

FIG. 1. (a) Left panel: schematics of a bilayer hexagonal lattice with four sites in the unit cell. Right panel: the first BZ and associated projected surface BZs. (b) Bulk band dispersions along the high-symmetry lines. (c) Surface state dispersions in the projected BZ in the k_x-k_y plane. The red (black) curves represent the dispersions of the surface (bulk) states. The plotted parameters in (b) and (c) are chosen as $t_0 = -1$, $m_0 = -0.5$, $t_1 = -0.8$, and $t_2 = -1.2$ in arbitrary unit (a.u.). (d) Schematics of the hinge states. The left panel, middle, and right panel show hinge state along the x direction in the top (blue arrows) and bottom (green arrows) surfaces, the x and z (red arrows) directions, and three independent directions, respectively.

m_0, while the other sites have the opposite value. At each layer, the nearest-neighbor hoppings, labeled by t_0 (gray tubes), occur for both the sublattices A and B, while for two adjacent layers, the hoppings, denoted, respectively, by t_1 (yellow tubes) and t_2 (cyan tubes), emerge only for the sublattice A. In the basis of (A_1, B_1, A_2, B_2), the Bloch Hamiltonian

$$\mathcal{H}(\mathbf{k}) = f_1\sigma_x + f_2\sigma_2 + m_0\sigma_z\tau_z + g_1(\sigma_z + \sigma_0)\tau_x + g_2(\sigma_z + \sigma_0)\tau_y, \qquad (1)$$

with $f_1 = t_0[1 + 2\cos(\sqrt{3}k_y/2)(\cos k_x/2)]$, $f_2 = 2t_0 \sin(\sqrt{3}k_y/2)\cos(k_x/2)$, $g_1 = (t_1 + t_2\cos k_z)/2$, and $g_2 = -t_2 \sin(k_z/2)$, where $\mathbf{k} = (k_x, k_y, k_z)$ is the Bloch wave vector, and a and h are the lattice constants in the x-y plane and along the z direction, respectively. σ_i and τ_i ($i = x, y, z$) are the Pauli matrices acting on the sublattice and layer degrees of freedom, respectively. The right panel in Fig. 1(a) shows the first Brillouin zone (BZ) and its projected surface BZs in the k_x-k_y and k_x-k_z planes.

Because of the breaking of the sublattice symmetry and the mirror symmetry along the z direction, the bulk band of the Hamiltonian (1) opens a gap between the first and second bands at the point H (or H'), as shown in Fig. 1(b). This gap closes for $t_1 = t_2$. In the case of $t_1 < t_2$, this Hamiltonian has gapped surface states in the k_x-k_y plane [red lines in Fig. 1(c)], which have the energy extreme at the valley $\bar{K}$ (or $\bar{K}'$). These surface states are located, respectively, on the top and bottom surfaces and share identical dispersions. For the top one, they are governed, near $\bar{K}$, by an effective Hamiltonian $\mathcal{H}_s = v_s(\bar{q}_x\sigma_x + \bar{q}_y\sigma_y) + m_s\sigma_z$, where $v_s = (\sqrt{3}t_0/2)\times\sqrt{1-(t_1/t_2)^2}$, $m_s = m_0$ is the effective mass, and $\bar{q}_x$ and $\bar{q}_y$ are the infinitesimal momenta [40]. This effective Hamiltonian supports a valley Chern number $C_{\bar{K}} = \mathrm{sgn}(m_s)/2$. Since the effective mass can be well tuned by controlling the on-site energies, we can introduce two phases I and II with the opposite effective masses, i.e., $\pm m_s$. When these two phases touch at the x-z plane [left panel of Fig. 1(d)], the hinge states along the x direction in the top surface (blue arrows) are formed by the Jackiw-Rebbi mechanism [39]. These hinge states are protected by an integer topological invariant $\Delta C_{\bar{K}} = \mathrm{sgn}(m_s)$ [13], and are dominated by an effective Hamiltonian $\mathcal{H}_h^x = v_s\bar{q}_x s_z$, where s_z is the Pauli matrix acting on the valley degree of freedom [40]. This effective Hamiltonian demonstrates the helical property of the hinge states, which can also be verified from their dispersions [40]. The hinge states in the bottom surface (green arrows) are the same as those in the top surface, but with an opposite topological invariant. Similarly, the hinge states along the y direction can also be produced when these two phases touch at the y-z plane.

Note that when I and II touch, there also exists gapped interface states, which have the energy extreme at the valley $\bar{H}$ (or $\bar{H}'$) [40]. In the vicinity of $\bar{H}$, they are dominated by an effective Hamiltonian $\mathcal{H}_{\text{I-II}} = \sqrt{3}t_0\bar{q}_x'\tau_x/2 + t_2\bar{q}_z'\tau_y/2 + m_{\text{I-II}}\tau_z$, where $\bar{q}_x'$ and $\bar{q}_z'$ are the infinitesimal momenta, $m_{\text{I-II}} = (t_1 - t_2)/2 < 0$ is also the effective mass controlled here by the interlayer couplings [40]. In this case, a valley

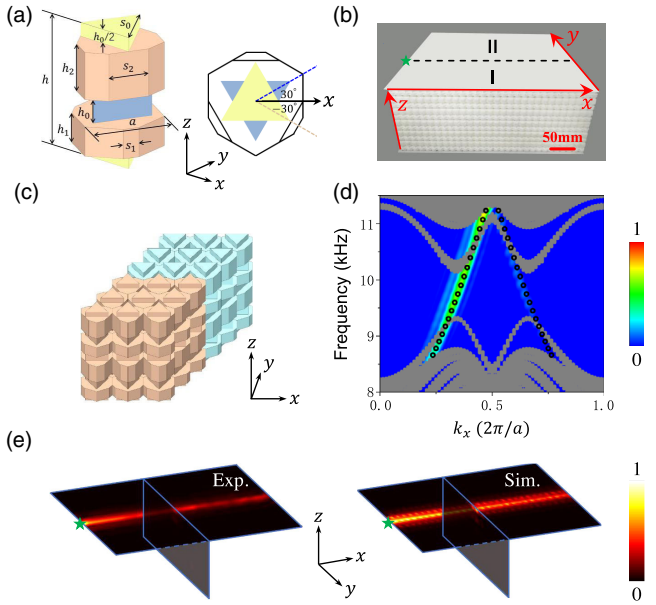

FIG. 2. (a) The side (left panel) and top (right panel) views of the unit cell for I. (b) A photo of the 3D printing PC sample. (c) The schematic structure of the PC sample. (d) Projected band dispersions along the k_x direction in the top surface. The color maps represent the experimental data, while the black (gray) circles reflect the simulated results of the hinge (bulk and surface) states. (e) Measured (left panel) and simulated (right panel) acoustic pressure field distributions of the hinge states at $f_e = 10.0$ kHz. The green stars denote the positions of the point source.

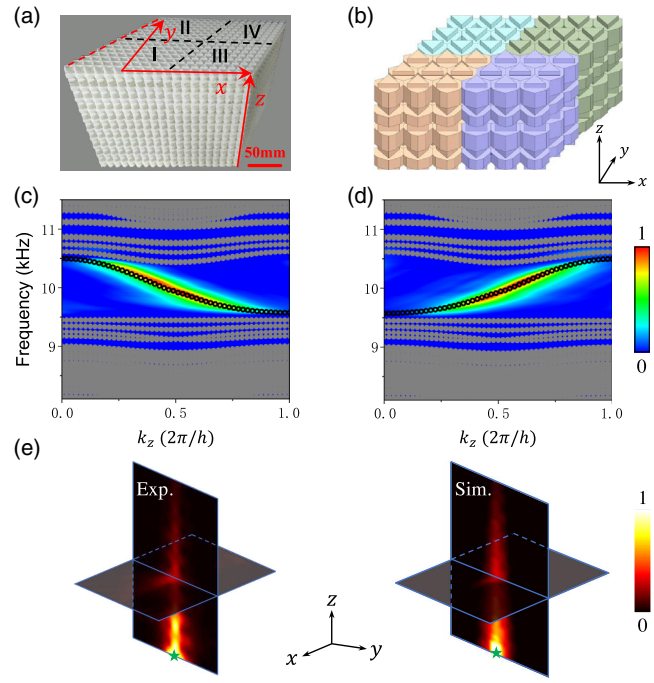

FIG. 3. (a) A photo of the 3D-printing PC sample with four phases I, II, III, and IV. (b) Schematic structure of the PC sample. (c) and (d) Projected band dispersions along the k_z direction, when the point sources are placed at the top and bottom surfaces, respectively. The color maps represent the experimental data, while the black (gray) circles reflect the simulated results of the hinge (bulk and surface) states. (e) Measured (left panel) and simulated (right panel) acoustic pressure field distributions of the hinge states at $f_e = 10.0$ kHz. The green star denotes the position of the point source.

Chern number $C_{\bar{H}} = -1/2$. We further introduce two extra phases III and IV, in which III (IV) has a similar property as that of the phase I (II) but with $t_1 > t_2$. When III and IV touch also at the x-z plane, similar interface states emerge and have an effective mass $m_{\text{III-IV}} = (t_1 - t_2)/2 > 0$. Since $m_{\text{I-II}} < 0$ and $m_{\text{III-IV}} > 0$, when the interfaces of I-II and III-IV touch [middle of Fig. 1(d)], the helical hinge states along the z direction (red arrows) are also produced by the Jackiw-Rebbi mechanism [39]. They are protected by an integer topological invariant $|\Delta C_{\bar{H}}| = 1$ [13] and are governed by an effective Hamiltonian $\mathcal{H}_h^z = t_2 \bar{q}_z' s_z/2$. The corresponding dispersions are plotted in Ref. [40].

Since the on-site energy of I (II) has the same as that of III (IV), no interface states of I-III and II-IV emerge. Also, for $t_1 > t_2$ in III and IV, no surface states in the k_x-k_y plane can be found. As a result, for the structure in the middle of Fig. 1(d), the hinge states only along the x and z directions can be produced. Fortunately, by introducing an L-shaped design for II based on the above structure, the hinge states along all the three independent directions can be achieved successfully, as shown by the right panel in Fig. 1(d). Notice that all the interfaces are here designed as the zigzag type, the new hinge states are generated along the direction that has 30° with respect to the y axis. Considering that all the hinge states are originated from the same effective Hamiltonian near the H point, reflections are greatly suppressed since the reflected modes are associated with different valleys [13,41], which indicates the emergence of 3D robust one-way hinge transports.

We now experimentally verify our findings in PCs. Figure 2(a) shows the side (left panel) and top (right panel) views of a unit cell for I. This bilayer hexagonal unit cell is formed by two triangular prism scatterers, which have the same side length ($s_0 = 12.85$ mm) and height ($h_0 = 6.00$ mm), but opposite rotation angles, 30°, with respect to the x axis. Two types of the triangular holes are drilled through the neighboring supporting plates with the side lengths and heights, $s_1 = 3.46$, $h_1 = 6.50$ mm and $s_2 = 8.66$, $h_2 = 10.40$ mm. The lattice constants $a = 17.32$ and $h = 28.90$ mm. The unit cell of II has the same as that of I but with the opposite rotation angle for each layer, while the unit cell of III (IV) is the same as that of I (II) but with different $s_1 = 8.66$ and $s_2 = 3.46$ mm. Note that the PCs can well capture the underlying physics of the tight-binding model introduced [40].

We first observe the hinge transport along the x direction. Using the 3D printing technology with the stereo lithography appearance, a PC sample with $30 \times 15 \times 6$ unit cells is fabricated by the plastic stereolithography material, as

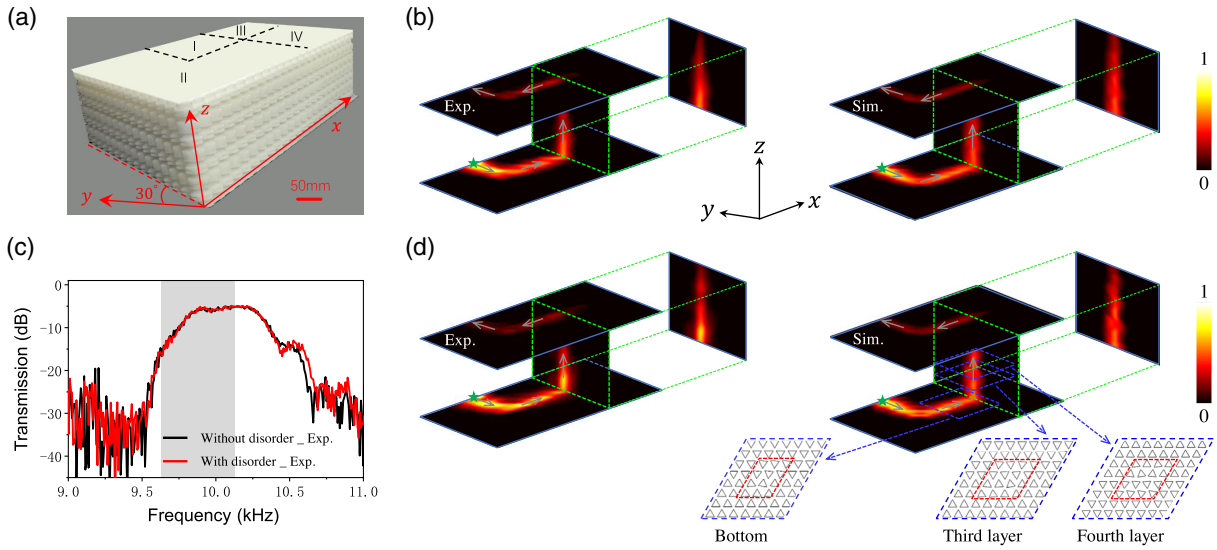

FIG. 4. (a) A photo of the printing PC sample with an L-shaped design for II. (b) Measured (left panel) and simulated (right panel) acoustic pressure field distributions at $f_e = 10.0$ kHz. The gray-arrowed lines reflect the one-way transport of the sound wave along the hinges of the sample. The green stars denote the positions of the point source. (c) Measured transmissions with (red curve) and without (black curve) two cases of the weak disorders. The shadowed region indicates the overlapped band gap of the surface and interface states. (d) Measured (left panel) and simulated (right panel) acoustic pressure field distributions at $f_e = 10.0$ kHz with the disorders in (c). The disorders are generated by rotating randomly the scatterers at the range of $\pm 10°$, and located, respectively, in the bottom surface and in the third and fourth layers, as shown by red boxes in the right panel of (d).

shown in Fig. 2(b). Figure 2(c) reflects the structure of this PC sample by stacking the unit cells of I and II along the z direction. Since the PC sample has two hinge states located, respectively, in the top and bottom surfaces, we should separately measure the acoustic pressure fields of these surfaces. A subwavelength headphone acted as a point source is placed at the left end (green star) to excite the hinge state in the top surface. A subwavelength microphone acted as a receiver is inserted into the sample to measure the acoustic pressure field [40]. By Fourier transforming the measured acoustic pressure fields, the hinge state dispersion along the k_x direction is obtained in Fig. 2(d). The left panel in Fig. 2(e) presents the measured acoustic pressure fields at the excitation frequency $f_e = 10.0$ kHz. It shows that the sound wave propagates to the right end along the hinge in the top surface and decays rapidly in the vertical plane. The experimental data agree well with the full-wave simulations, as shown by the right panel in Fig. 2(e). If the point source is placed at the right end, the sound wave propagates to the left end at the same excitation frequency [40], which, together with Fig. 2(e), verifies the helical property of the hinge states. Furthermore, the hinge states in the bottom surface are similar to those in the top surface [40].

We then observe the hinge transport along the z direction by printing another PC sample with $20 \times 16 \times 14$ unit cells shown in Fig. 3(a). The corresponding structure is illustrated in Fig. 3(b). This PC sample is constituted by four phases I, II, III, and IV. When the point source is placed at the intersection point of the four phases in the top surface, the measured hinge state dispersion along the k_z direction is shown by colors in Fig. 3(c). Because of the helical property, the hinge state can also be excited by the point source in the bottom surface and the corresponding dispersion is measured in Fig. 3(d). The observed dispersions match well those of the simulation. In Fig. 3(e), we observe (left panel) and simulate (right panel) the acoustic pressure fields at $f_e = 10.0$ kHz, showing that the sound wave propagates from the bottom to the top along the hinge of the z direction.

Finally, we observe 3D hinge transport by printing a PC sample with $24 \times 16 \times 4$ unit cells shown in Fig. 4(a). By placing the point source at the bottom surface, we measure the acoustic pressure field distributions in the top and bottom surfaces as well as the interfaces of I-III and II-IV. The left panel of Fig. 4(b) presents the experimental data at $f_e = 10.0$ kHz. It shows that the sound wave first propagates along the hinge of the bottom x-y plane, then turns into the hinge of the z direction, and finally travels along the hinge of the top x-y plane (gray-arrowed lines). This experimental observation, matching with the simulation shown by the right panel of Fig. 4(b), demonstrates definitely the 3D hinge transport, as expected.

In Fig. 4(c), we also measure the transmissions for the weak disorder to demonstrate the robustness of the 3D hinge transport. The weak disorder is generated by rotating randomly the scatterers at the range of $\pm 10°$ and has two cases. One is in the bottom surface and the other is in the third and fourth layers, as shown by red boxes in the right panel of Fig. 4(d). At this time, the point source and the

receiver are placed at the incident port on the bottom surface and outgoing port on the top surface, respectively. The red (black) curve of Fig. 4(c) shows the experimental data with (without) these disorders. These curves show that for the weak disorders, the transmissions within the frequency range of $9.6 \sim 10.1$ kHz remain consistent. Figure 4(d) presents the measured (left panel) and simulated (right panel) acoustic pressure field distributions at the excitation frequency of 10.0 kHz, which again shows that the weak disorders hardly affect the multichannel hinge transport. The results in Figs. 4(c) and 4(d) clearly verify the robustness of the 3D hinge transport. This is a universal property caused by the intrinsic topological feature of the acoustic TIs.

In summary, we have theoretically predicted, numerically simulated, and experimentally observed the helical hinge states along three independent directions in a higher-order TI. The 3D robust one-way transport from hinge to hinge has been realized successfully, which is in sharp contrast to the recent works about the higher-order topological semimetals with only 1D hinge transport [42–46]. This novel sound transport may serve as the basis for acoustic devices of unconventional functions [47].

This work is supported by the National Key R & D Program of China (Grants No. 2017YFA0304203 and No. 2018YFA0305800), the National Natural Science Foundation of China (Grants No. 11890701, No. 11974120, No. 11974005, No. 12034012, No. 12074128, No. 12074232, and No. 12125406), and Shanxi 1331 Project Key Subjects Construction.

Q. W. and X. Z. contributed equally to this work

*Corresponding author.
chengang971@163.com
†Corresponding author.
zyliu@whu.edu.cn

[1] J.-C. Charlier, X. Blas, and S. Roche, Electronic and transport properties of nanotubes, Rev. Mod. Phys. **79**, 677 (2007).
[2] R. B. Schoch, J. Han, and P. Renaud, Transport phenomena in nanofluidics, Rev. Mod. Phys. **80**, 839 (2008).
[3] S. D. Sarma, S. Adam, E. H. Hwang, and E. Rossi, Electronic transport in two-dimensional graphene, Rev. Mod. Phys. **83**, 407 (2011).
[4] E. A. Laird, F. Kuemmeth, G. A. Steele, K. Grove-Rasmussen, J. Nygard, K. Flensberg, and L. P. Kouwenhoven, Quantum transport in carbon nanotubes, Rev. Mod. Phys. **87**, 703 (2015).
[5] M. Knig, S. Wiedmann, C. Brne, A. Roth, H. Buhmann, L. W. Molenkamp, X.-L. Qi, and S.-C. Zhang, Quantum spin hall insulator state in HgTe quantum wells, Science **318**, 766 (2007).
[6] M. Z. Hasan and C. L. Kane, Colloquium: Topological insulators, Rev. Mod. Phys. **82**, 3045 (2010).
[7] X.-L. Qi and S.-C. Zhang, Topological insulators and superconductors, Rev. Mod. Phys. **83**, 1057 (2011).
[8] T. Ozawa, H. M. Price, A. Amo, N. Goldman, M. Hafezi, L. Lu, M. C. Rechtsman, D. Schuster, J. Simon, O. Zilberberg, and I. Carusotto, Topological photonics, Rev. Mod. Phys. **91**, 015006 (2019).
[9] Y. Yang, Z. Gao, H. Xue, L. Zhang, M. He, Z. Yang, R. Singh, Y. Chong, B. Zhang, and H. Chen, Realization of a three-dimensional photonic topological insulator, Nature (London) **565**, 622 (2019).
[10] Y. Yang, Y. F. Xu, T. Xu, H.-X. Wang, J.-H. Jiang, X. Hu, and Z. H. Hang, Visualization of a Unidirectional Electromagnetic Waveguide Using Topological Photonic Crystals Made of Dielectric Materials, Phys. Rev. Lett. **120**, 217401 (2018).
[11] Z. Gao, Z. Yang, F. Gao, H. Xue, Y. Yang, J. Dong, and B. Zhang, Valley surface-wave photonic crystal and its bulk/edge transport, Phys. Rev. B **96**, 201402(R) (2017).
[12] C. He, X. Ni, H. Ge, X. C. Sun, Y. B. Chen, M. H. Lu, X. P. Liu, and Y. F. Chen, Acoustic topological insulator and robust one-way sound transport, Nat. Phys. **12**, 1124 (2016).
[13] J. Lu, C. Qiu, L. Ye, X. Fan, M. Ke, F. Zhang, and Z. Liu, Observation of topological valley transport of sound in sonic crystals, Nat. Phys. **13**, 369 (2017).
[14] M. Miniaci, R. K. Pal, B. Morvan, and M. Ruzzene, Experimental Observation of Topologically Protected Helical Edge Modes in Patterned Elastic Plates, Phys. Rev. X **8**, 031074 (2018).
[15] J. Cha, K. W. Kim, and C. Daraio, Experimental realization of on-chip topological nanoelectromechanical metamaterials, Nature (London) **564**, 229 (2018).
[16] L.-C. Chen, P.-Q. Chen, W.-J. Li, and X.-J. Chen, Enhancement of thermoelectric performance across the topological phase transition in dense lead selenide, Nat. Mater. **18**, 1321 (2019).
[17] F. Han, N. Andrejevic, T. Nguyen, V. Kozii, Q. T. Nguyen, T. Hogan, Z. Ding, R. Pablo-Pedro, S. Parjan, B. Skinner, A. Alatas, E. Alp, S. Chi, J. Fernandez-Baca, S. Huang, L. Fu, and M. Li, Quantized thermoelectric Hall effect induces giant power factor in a topological semimetal, Nat. Commun. **11**, 6167 (2020).
[18] H. He, C. Qiu, L. Ye, X. Cai, X. Fan, M. Ke, F. Zhang, and Z. Liu, Topological negative refraction of surface acoustic waves in a Weyl phononic crystal, Nature (London) **560**, 61 (2018).
[19] Y. Yang, H. X. Sun, J. P. Xia, H. Xue, Z. Gao, Y. Ge, D. Jia, S. Q Yuan, Y. Chong, and B. Zhang, Topological triply degenerate point with double Fermi arcs, Nat. Phys. **15**, 645 (2019).
[20] M. A. Bandres, S. Wittek, G. Harari, M. Parto, J. Ren, M. Segev, D. N. Christodoulides, and M. Khajavikhan, Topological insulator laser: Experiments, Science **359**, eaar4005 (2018).
[21] W. A. Benalcazar, B. A. Bernevig, and T. L. Hughes, Quantized electric multipole insulators, Science **357**, 61 (2017).
[22] W. A. Benalcazar, B. A. Bernevig, and T. L. Hughes, Electric multipole moments, topological multipole moment pumping, and chiral hinge states in crystalline insulators, Phys. Rev. B **96**, 245115 (2017).

[23] Z. Song, Z. Fang, and C. Fang, (d-2)-Dimensional Edge States of Rotation Symmetry Protected Topological States, Phys. Rev. Lett. **119**, 246402 (2017).
[24] M. Ezawa, Higher-Order Topological Insulators and Semimetals on the Breathing Kagome and Pyrochlore Lattices, Phys. Rev. Lett. **120**, 026801 (2018).
[25] D. Calugaru, V. Juricic, and B. Roy, Higher-order topological phases: A general principle of construction, Phys. Rev. B **99**, 041301(R) (2019).
[26] A. Saha and A. M. Jayannavar, Higher order topological systems: A new paradigm, arXiv:2107.00847 (2021).
[27] F. Schindler, A. M. Cook, M. G. Vergniory, Z. Wang, S. S. P. Parkin, B. A. Bernevig, and T. Neupert, Higher-order topological insulators, Sci. Adv. **4**, eaat0346 (2018).
[28] C. He, H. S. Lai, B. He, S. Y. Yu, X. Xu, M. H. Lu, and Y. F. Chen, Acoustic analogues of three-dimensional topological insulators, Nat. Commun. **11**, 2318 (2020).
[29] R. Noguchi *et al.*, Evidence for a higher-order topological insulator in a three-dimensional material built from van der Waals stacking of bismuth-halide chains, Nat. Mater. **20**, 473 (2021).
[30] J. Langbehn, Y. Peng, L. Trifunovic, F. Oppen, and P. W. Brouwer, Reflection-Symmetric Second-Order Topological Insulators and Superconductors, Phys. Rev. Lett. **119**, 246401 (2017).
[31] S. H. Kooi, G. Miert, and C. Ortix, Inversion-symmetry protected chiral hinge states in stacks of doped quantum Hall layers, Phys. Rev. B **98**, 245102 (2018).
[32] E. Khalaf, Higher-order topological insulators and superconductors protected by inversion symmetry, Phys. Rev. B **97**, 205136 (2018).
[33] G. Miert and C. Ortix, Higher-order topological insulators protected by inversion and rotoinversion symmetries, Phys. Rev. B **98**, 081110(R) (2018).
[34] X. Ni, Z. Xiao, A. B. Khanikaev, and A. Alù, Robust Multiplexing with Topolectrical Higher-Order Chern Insulators, Phys. Rev. Applied **13**, 064031 (2020).
[35] K. Plekhanov, F. Ronetti, D. Loss, and J. Klinovaja, Hinge states in a system of coupled Rashba layers, Phys. Rev. Research **2**, 013083 (2020).
[36] T. Nag, V. Juricic, and B. Roy, Hierarchy of higher-order Floquet topological phases in three dimensions, Phys. Rev. B **103**, 115308 (2021).
[37] A. Mook, S. A. Daz, J. Klinovaja, and D. Loss, Chiral hinge magnons in second-order topological magnon insulators, Phys. Rev. B **104**, 024406(R) (2021).
[38] F. Schindler, Z. Wang, M. G. Vergniory, A. M. Cook, A. Murani, S. Sengupta, A. Y. Kasumov, R. Deblock, S. Jeon, I. Drozdov, H. Bouchiat, S. Guron, A. Yazdani, B. A. Bernevig, and T. Neupert, Higher-order topology in bismuth, Nat. Phys. **14**, 918 (2018).
[39] R. Jackiw and C. Rebbi, Solitons with fermion number 1/2, Phys. Rev. D **13**, 3398 (1976).
[40] See Supplemental Material http://link.aps.org/supplemental/10.1103/PhysRevLett.127.255501 for more details on the derivation of effective Hamiltonian and hinge states, the numerical simulations and experimental measurements, the correspondence between the PC and the tight-binding model, and the influence of the viscothermal losses on the transmission.
[41] J.-W. Dong, X.-D. Chen, H. Zhu, Y. Wang, and X. Zhang, Valley photonic crystals for control of spin and topology, Nat. Mater. **16**, 298 (2017).
[42] H.-X. Wang, Z.-K. Lin, B. Jiang, G.-Y. Guo, and J.-H. Jiang, Higher-Order Weyl Semimetals, Phys. Rev. Lett. **125**, 146401 (2020).
[43] Sayed Ali Akbar Ghorashi, T. Li, and T. L. Hughes, Higher-Order Weyl Semimetals, Phys. Rev. Lett. **125**, 266804 (2020).
[44] Q. Wei, X. Zhang, W. Deng, J. Lu, X. Huang, M. Yan, G. Chen, Z. Liu, and S. Jia, Higher-order topological semimetal in acoustic crystals, Nat. Mater. **20**, 812 (2021).
[45] L. Luo, H.-X. Wang, Z.-K. Lin, B. Jiang, Y. Wu, F. Li, and J.-H. Jiang, Observation of a phononic higher-order Weyl semimetal, Nat. Mater. **20**, 794 (2021).
[46] Z.-Q. Zhang, B.-L. Wu, C.-Z. Chen, and H. Jiang, The global phase diagram of disordered higher-order Weyl semimetals, Phys. Rev. B **104**, 014203 (2021).
[47] C.-A. Li, S.-B. Zhang, J. Li, and B. Trauzettel, Higher-Order Fabry-Prot Interferometer from Topological Hinge States, Phys. Rev. Lett. **127**, 026803 (2021).